Article

Toward Complete Optical Coupling to Confined Surface Polaritons

Published as part of ACS Photonics virtual special issue "Frontiers and Applications of Plasmonics and Nanophotonics".

Saad Abdullah, Eduardo J. C. Dias, Jan Krpenský, Vahagn Mkhitaryan,* and F. Javier García de Abajo*

Cite This: *ACS Photonics* 2024, 11, 2183−2193
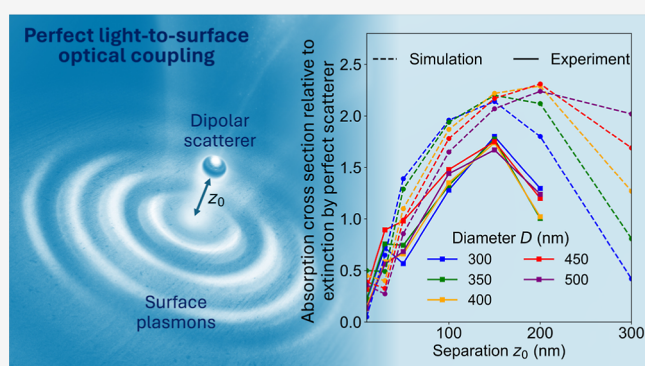
Read Online

ACCESS | Metrics & More | Article Recommendations | SI Supporting Information

ABSTRACT: Optical coupling between propagating light and confined surface polaritons plays a pivotal role in the practical design of nanophotonic devices. However, the coupling efficiency decreases dramatically with the degree of mode confinement due to the mismatch that exists between the light and polariton wavelengths, and despite the intense efforts made to explore different mechanisms proposed to circumvent this problem, the realization of a flexible scheme to efficiently couple light to polaritons remains a challenge. Here, we experimentally demonstrate an efficient coupling of light to surface−plasmon polaritons assisted by engineered dipolar scatterers placed at an optimum distance from the surface. Specifically, we fabricate gold disks separated by a silica spacer from a planar gold surface and seek to achieve perfect coupling conditions by tuning the spacer thickness for a given scatterer geometry that resonates at a designated optical frequency. We measure a maximum light-to-plasmon coupling cross section of the order of the square of the light wavelength at an optimum distance that results from the interplay between a large particle-surface interaction and a small degree of surface-driven particle-dipole quenching, both of which are favored at small separations. Our experiments, in agreement with both analytical theory and electromagnetic simulations, support the use of optimally placed engineered scatterers as a disruptive approach to solving the long-standing problem of in/out-coupling in nanophotonics.

KEYWORDS: polaritonics, complete optical coupling, nanoparticles, lattice resonances, particle arrays, complete absorption

Perfect light-to-surface optical coupling. Dipolar scatterer, z_0. Surface plasmons. Absorption cross section relative to extinction by perfect scatterer vs Separation z_0 (nm). Simulation (dashed), Experiment (solid). Diameter D (nm): 300, 350, 400, 450, 500.

INTRODUCTION

The ability to confine and manipulate light at small length scales allows us to enhance the optical electromagnetic field by several orders of magnitude at specific spatial locations, and this, in turn, enables the design of improved optoelectronic devices,[1,2] chemical sensors,[3−5] and nonlinear photonic structures.[6−8] Surface polaritons play an important role in this context because they provide the means to realize a strong degree of spatial confinement, thanks to their small associated wavelengths compared with the light wavelength at the same frequency. In particular, visible and near-infrared plasmons can be trapped in regions spanning just a few nanometers in size,[9] resulting in a large field enhancement that has been extensively leveraged for optical sensing and chemical identification[5,10] down to the single-molecule level[11−13] as well as for enhancing both the efficiency of light harvesters[14,15] and the nonlinear response of nanostructures.[7,16] As impressive as these applications might be, the full potential of light confinement is dramatically hindered by the mismatch between the light and polariton wavelengths, which results in an intrinsically weak in and out coupling of propagating light to polaritons[17] and prevents a wider deployment of polariton-based devices.

The problem of exciting ultraconfined polaritons is commonly addressed by the following two different kinds of strategies: the inelastic conversion of energy into polaritons and the transformation of incident photons into polaritons. Among the former, localized emitters such as quantum dots can be placed at designated positions and be optically or electrically excited, so they decay into single polaritons with a good quantum efficiency.[18,19] Inelastic electron tunneling from metallic tips[20,21] and heterojunctions[22] can also lead to the generation of polaritons. Likewise, free electrons are routinely used to create polaritons with a high degree of control over their spatial placement in the context of electron microscopy,[23,24] and in fact, this approach enabled pioneer studies in plasmonics.[25,26] Although these methods can be made
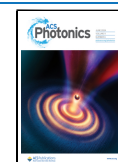
efficient,[19,27] alternative schemes based on the direct coupling from light to polaritons hold the advantage of preserving optical coherence, thus enabling a vast range of applications in which interference and phase information play a role.[28,29] For moderately confined surface polaritons, the prism-based Kretschmann configuration[30,31] provides an efficient coupling method, which unfortunately cannot be extrapolated to strongly confined modes as they would require the use of prisms with a high refractive index of the order of λ/λ_p (the ratio of the free-space photon and polariton wavelengths). Consequently, optical coupling generally relies on scattering elements such as surface edges,[28,32] nanotips,[33,34] and gratings,[35,36] whose efficiencies are limited by the polariton-light wavelength mismatch mentioned above.

A dipolar scatterer constitutes a prototypical element that can assist in light-to-polariton coupling. Surface polaritons decay evanescently away from the supporting medium, and therefore, the interaction between a scatterer and surface polaritons increases as their separation is reduced. However, that interaction also contributes to quenching the excitation of the scatterer by incident light, which is detrimental to coupling. A rigorous analysis leads to a fundamental limit for the maximum achievable light-to-polariton coupling cross section at short scatterer–surface separations:[17] the maximum possible in-coupling cross section is $\sim\lambda_p^3/\lambda$, where λ_p and λ are the polariton and photon wavelengths, respectively. For strongly confined surface modes ($\lambda_p \ll \lambda$), the cross section is thus very small compared with the free-space extinction cross section of a resonant lossless dipolar scatterer, $\sigma_0 = 3\lambda^2/2\pi$. This situation can be improved by separating the scatterer from the surface to find the optimum balance between an intense scatterer–polariton interaction (favored at short separations) and a small surface quenching (decreasing with an increasing scatterer–surface distance). Based on this concept, complete coupling between focused light beams and surface polaritons has been predicted to be possible through precise adjustment of the distance between the scatterer and the surface and, in addition, shaping the angular profile of the incident light such that it matches that associated with the emission from the dipolar scatterer in the presence of the surface.[37] Likewise, one expects that the coupling cross section under plane wave incidence conditions can be substantially increased by using resonant lossless scatterers placed at an optimum distance from the polaritonic surface, but this concept has not yet been experimentally explored.

In this work, we demonstrate an optimum coupling between light and surface modes in a planar gold-silica interface assisted by resonant dipolar scatterers separated from the metal by a silica spacer. Specifically, we fabricate gold disks that act as reasonably lossless scatterers placed at a controlled distance from the gold surface. Under plane-wave illumination, we measure coupling cross sections that exceed the free-space perfect-dipole extinction cross section $\sigma_0 = 3\lambda^2/2\pi$ by nearly a factor of 2, provided the disk resonates at the operation frequency and an optimum choice of the spacer thickness is made. The coupling cross section decreases from such a maximum value when the spacer thickness is varied and also at frequencies away from the scatterer resonance. Our results support the use of distant scatterers as a practical approach to solving the in/out-coupling problem in nanophotonics by efficiently funneling far-field radiation into surface polaritons at designated spatial positions on a flat surface.

■ RESULTS AND DISCUSSION

Light Coupling to a Planar Surface Assisted by a Dipolar Scatterer. A dipolar point scatterer represents a prototypical element that mediates light coupling to the optical modes of a planar surface. We discuss coupling to a metallic film under normal-incidence illumination (Figure 1a) and start
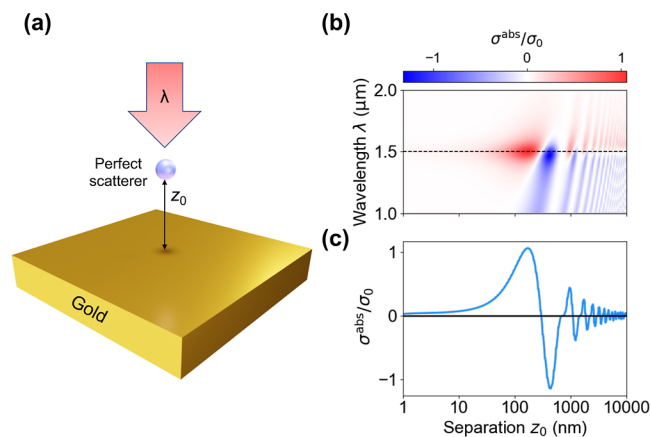

Figure 1. Optimizing the variation in absorption cross-section due to a dipole placed near a planar surface. (a) Scheme of the system under consideration, consisting of a dipolar scatterer placed at a distance z_0 from a gold surface under normal-incidence plane-wave illumination at wavelength λ. (b) Calculated variation of the absorption cross section σ^{abs} due to the presence of the scatterer as a function of light wavelength λ and dipole–surface separation z_0. The scatterer is taken to be lossless and resonant at a wavelength $\lambda_0 = 1.5~\mu$m, with a resonance width $\kappa = 0.1 \times 2\pi c/\lambda_0$. We normalize σ^{abs} to the maximum dipolar extinction cross-section in free space, $\sigma_0 = 3\lambda^2/2\pi$. (c) Cut of σ^{abs} along the dashed line in panel (b) at fixed wavelength $\lambda = \lambda_0$.

by first considering a lossless scatterer described by a Lorentzian polarizability

$$\alpha(\omega) \approx \frac{3c^3}{4\omega_0^3} \frac{\kappa}{\omega_0 - \omega - i\kappa/2} \qquad (1)$$

which is resonant at a frequency ω_0 (wavelength $\lambda_0 = 2\pi c/\omega_0$) with a total width κ. The $i\kappa/2$ term in the denominator relates to all light–particle interaction processes (elastic scattering and inelastic absorption), while the presence of κ in the numerator guarantees that inelastic absorption in vacuum ($\propto\text{Im}\{\alpha\} - |\alpha|^2 2\omega^3/3c^3$) vanishes at $\omega = \omega_0$. This system can be described analytically, as shown in the Methods section. In Figure 1b,c, we present the change in the absorption cross section of the entire system produced by the presence of the particle (i.e., the difference between extinction and scattering cross sections, $\sigma^{abs} = \sigma^{ext} - \sigma^{scat}$, using the explicit expressions in eqs 17a and 17b; see Figure S1 in the Supporting Information for plots of σ^{ext} and σ^{scat}). We take $\kappa = 0.1~\omega_0$ as a reasonable radiation-limited nanoparticle resonance width (compatible with experimental data in Figure S3 in the Supporting Information) and find that σ^{abs} varies dramatically with the dipole-surface separation. We find it natural to compare the cross section associated with the particle-near-a-surface system to the maximum extinction cross section of a dipolar scatterer in free space σ_0. Specifically, we find that the absolute variation of σ^{abs} goes from $-1.32~\sigma_0$ to $1.06~\sigma_0$ (i.e., exceeding σ_0 for some dipole-surface separations within the 100−500 nm range). This is more clearly illustrated in a cut of the contour plot for fixed wavelength $\lambda = \lambda_0$ (Figure 1c), which also reveals the presence of alternating maxima and
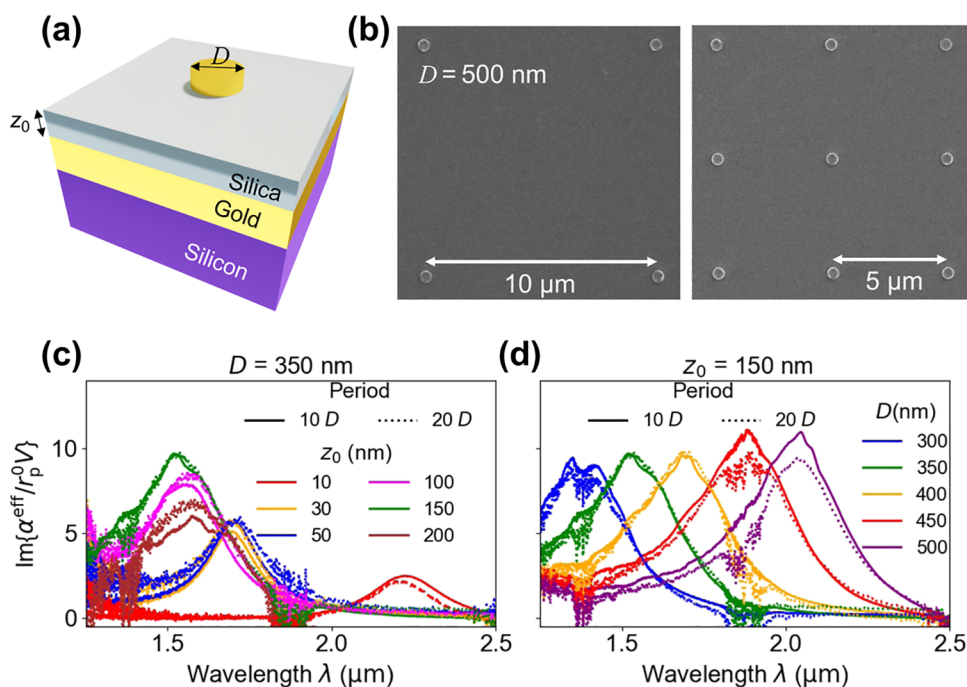
Figure 2. Measurement of the effective polarizability of a single disk near a metal surface. (a) Schematic representation of the samples under consideration, consisting of gold disks of diameter D and height $h = 40$ nm lying on a silica layer of thickness z_0 deposited on top of a 100 nm-thick gold film. (b) SEM images of two of the fabricated samples with $D = 500$ nm disks arranged in sparse square periodic arrays of periods $a = 20\,D$ (left) and $a = 10\,D$ (right). (c,d) Wavelength dependence of the effective polarizability $\mathrm{Im}\{\alpha^{\mathrm{eff}}/r_p^0 V\}$ extracted from experimental measurements and normalized by using the reflection coefficient r_p^0 of the planar surface (in the absence of particles) and the disk volume $V = \pi h D^2/4$ for either (c) fixed $D = 350$ nm and varying z_0 or (d) fixed $z_0 = 150$ nm and varying D. In each case, results obtained from samples with periods of $10\,D$ (solid curves) and $20\,D$ (broken curves) are shown.

minima oscillating between negative and positive values of σ^{abs}. Interestingly, the variation can be positive or negative, indicating a larger coupling to surface modes for $\sigma^{\mathrm{abs}} > 0$ and depletion of absorption by the planar surface (absorbance of ~98%) for $\sigma^{\mathrm{abs}} < 0$. We remark that σ^{abs} does not refer to the total absorption of the system but rather the variation of absorption due to the presence of the scatterer, so a negative value means that total absorption is reduced relative to the surface without scatterer. This behavior is the result of the interplay between different scattering field components, including the self-consistent dipole field induced by the incident light, its reflection on the surface, and the image dipole.

Experimental Demonstration of Optimum Scatterer-Assisted Light Coupling to Surface Plasmons. We experimentally explore the concept of particle-assisted optimum light coupling to surface modes by fabricating samples with the configuration sketched in Figure 2a (see the Methods section), consisting of gold disks (thickness $h = 40$ nm and varying diameter in the $D = 300-500$ nm range) separated by a silica layer (thickness $z_0 = 10-200$ nm) from an optically thick (100 nm) gold surface. The optical response is then measured for normal-incidence light impinging on the system from the upper side. Light coupling to gold surface modes (e.g., surface–plasmon polaritons) is assisted by the particles and translates into depletion of the reflectance, which we monitor through Fourier-transform infrared (FTIR) spectrometry. To obtain a sizable signal, we arrange the particles in periodic square arrays with a large period a, such that the interaction among particles can be safely neglected. In particular, for each particle diameter, D, we fabricate samples with periods given by either $a = 10\,D$ or $a = 20\,D$, as illustrated

by the scanning electron microscope (SEM) images presented in Figure 2b for $D = 500$ nm. The range of particle diameters is chosen such that the particle response is dominated by an in-plane dipolar plasmon within the spectral window under consideration (see Figure S2 in the Supporting Information). We assimilate the particle, including its interaction with the layered surface, to an effective polarizability $\alpha^{\mathrm{eff}}(\omega)$. The Fresnel reflection coefficient r_p^0 of the bare surface (without particles and considering p polarization for concreteness, as the results are polarization-independent under normal incidence on in-plane isotropic materials) is then supplemented by the field scattered from the particles. For small particles that can be described through a polarizability $\alpha(\omega)$, the effective polarizability is given by (see eq 11 in the Methods section)

$$\alpha^{\mathrm{eff}} = \frac{1}{\alpha^{-1} - \mathcal{G}} \qquad (2)$$

where $\mathcal{G}$ accounts for the interaction of the self-consistently induced dipole with the surface (eqs 8a). In our samples, the disks are relatively large compared with their separation from the gold–silica planar interface, so they cannot be described as point particles, but their response is still dominated by a dipolar mode (see Figure S2 in the Supporting Information), and therefore, it is legitimate to represent them through an effective polarizability $\alpha^{\mathrm{eff}}(\omega)$, which includes their interaction with the surface. Importantly, the combination of eqs 1 and 2 produces an expression for the effective polarizability similar to eq 1 but with an additional correction factor f in the numerator (see Section S2 in the Supporting Information), which we find to be of order unity in our fitting of the experimental results discussed below (see Figure S3 in the Supporting Information,
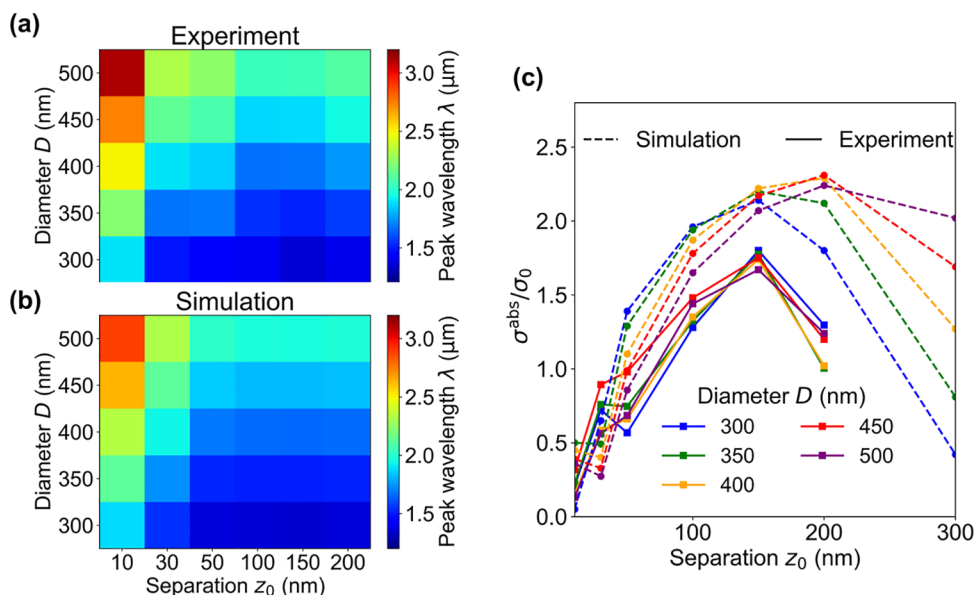
Figure 3. Coupling cross section of single disks to a metal surface. (a,b) Measured (a) and simulated (b) dependence of the wavelength for the maximum coupling cross section as a function of disk diameter D and silica spacing z_0 under the conditions of Figure 2a. (c) Maximum coupling cross section corresponding to the wavelengths in (a,b) as a function of silica spacing z_0 for different disk diameters D. The cross section is normalized to $\sigma_0 = 3\lambda_0^2/2\pi$.

where the fitted expression compares excellently with actual measured data). In addition, the obtained values of f are compatible with the condition that the variations in extinction and absorption cross sections of the particle–surface system are similar in magnitude (see Figure S4 in the Supporting Information).

Using previous results for periodic arrays of dipolar particles,[38] we can write the total specular reflection coefficient of the surface plus disks as $r = r_p^0 - 4\pi^2 i\alpha^{\mathrm{eff}}(\omega)/a^2\lambda$, where we neglect interparticle interactions because of the large in-plane separation a in our samples. Also for this reason, the second term in r is small compared with $|r_p^0| \lesssim 1$, so we can approximate the relative change in reflectivity (i.e., taking the bare surface as reference in the FTIR measurements) as

$$R = \left|r/r_p^0\right|^2 \approx 1 + (8\pi^2/a^2\lambda)\mathrm{Im}\{\alpha^{\mathrm{eff}}(\omega)/r_p^0\}$$

Plugging our measured values of R in this expression, we experimentally determine $\mathrm{Im}\{\alpha^{\mathrm{eff}}(\omega)/r_p^0\}$, whose spectral dependence is presented in Figure 2c,d. Reassuringly, we obtain very similar profiles for the normalized polarizability of the samples with the smallest and largest periods (solid and broken curves, respectively), thus corroborating our hypothesis of negligible interparticle interactions. The spectral profiles are dominated by the noted in-plane dipolar mode, whose peak position redshifts with increasing D (Figure 2d for fixed $z_0 = 150$ nm) as a manifestation of retardation in larger particles, which is further accompanied by an increase in the strength of the polarizability. The evolution with z_0 (Figure 2c for particles of diameter $D = 350$ nm) is more complex and characterized by frequency shifts associated with the particle-surface interaction. For a point-particle system, the maximum of the effective polarizability is roughly given by the condition $\mathrm{Re}\{\alpha^{-1} - \mathcal{G}\} = 0$ (see eq 2), which moves the resonance frequency from ω_0 in the isolated particle (see eq 1) to a new frequency ω. The attractive dipole-surface interaction generally produces $\omega < \omega_0$. We observe this effect in our experiments in

the $z_0 \sim 10-150$ nm range, although a small redshift with increasing z_0 takes place at larger separations, presumably as a result of the more complex particle–surface interaction due to the departure from the point-particle limit in the disks.

As expected from the analysis presented in Figure 1, the magnitude of the polarizability displays a maximum as a function of particle–metal separation, which is observed in our measurements at $z_0 \sim 150$ nm. Incidentally, the bare surface has a reflection coefficient $r_p^0 \approx 1$ within the investigated spectral range, and therefore, the spectral curves displayed in Figure 2c,d can be approximately regarded as those of the effective particle-on-the-surface polarizability.

The existence of a maximum in the obtained effective polarizability anticipates that the coupling cross section from incident light to surface modes should also find a maximum at some optimum distance. Here, we obtain the absorption cross section (dominated by coupling to surface modes) from the experimentally measured FTIR reflectivity R as $\sigma^{\mathrm{abs}} = (1 - R)a^2$ (i.e., the fraction of light that is depleted from the reflection signal multiplied by the unit cell area). We then search for the maximum cross section in the spectra as a function of D and z_0, which occurs at wavelengths in the near-infrared spectral range (Figure 3a) exhibiting a redshift when D is increased (as an effect of retardation) or z_0 decreased (as the result of the attractive coupling between the particle dipole and the surface) (see Figure S5 in the Supporting Information for the whole set of measured spectra of the cross section). This trend and the actual values of the maximum wavelength are well reproduced by the electromagnetic simulations plotted in Figure 3b.

Similar to the polarizability, the peak coupling cross section takes maximum values for a disk-gold surface separation $z_0 \sim 150$ nm (Figure 3c). This optimum distance is rather independent of the disk diameter (Figure S5 in the Supporting Information), although this parameter affects the spectral position of the particle resonance due to retardation for increasing size (Figure 3a,b). Incidentally, the absolute value of
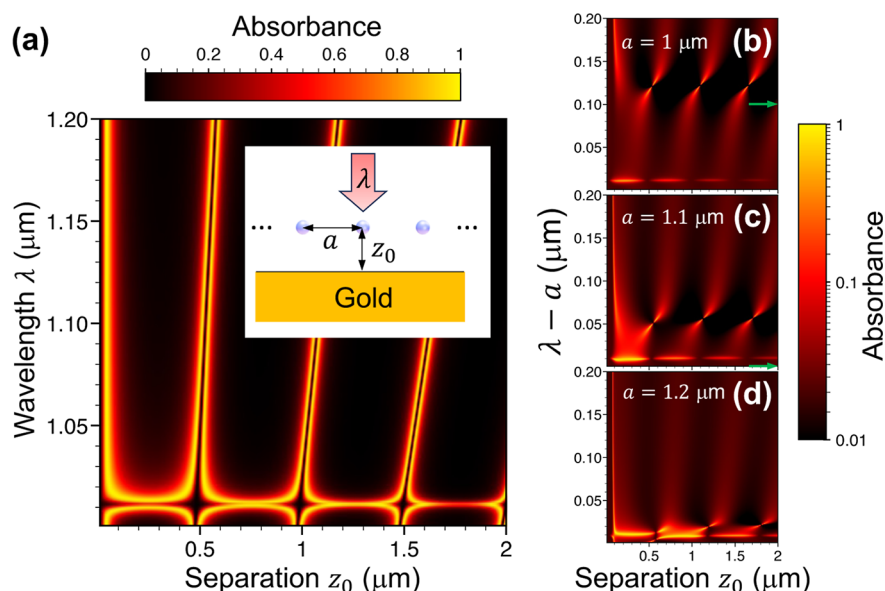
Figure 4. Resonant absorption by periodic particle arrays near a gold surface. (a) Absorbance under normal incidence on a square particle array as a function of particle−surface separation z_0 and light wavelength λ. We set the array period to $a = 1$ μm and the particle polarizability such that $\mathrm{Re}\{\alpha^{-1} - G\} = 0$ (resonant) and $\mathrm{Im}\{-\alpha^{-1}\} = 16\pi^3/3\lambda^3$ (lossless). (b−d) Same as (a) for different periods a (see labels) and particles described by the polarizability of eq 1 with a resonance wavelength of $\lambda_0 = 1.1$ μm (indicated by green arrows).
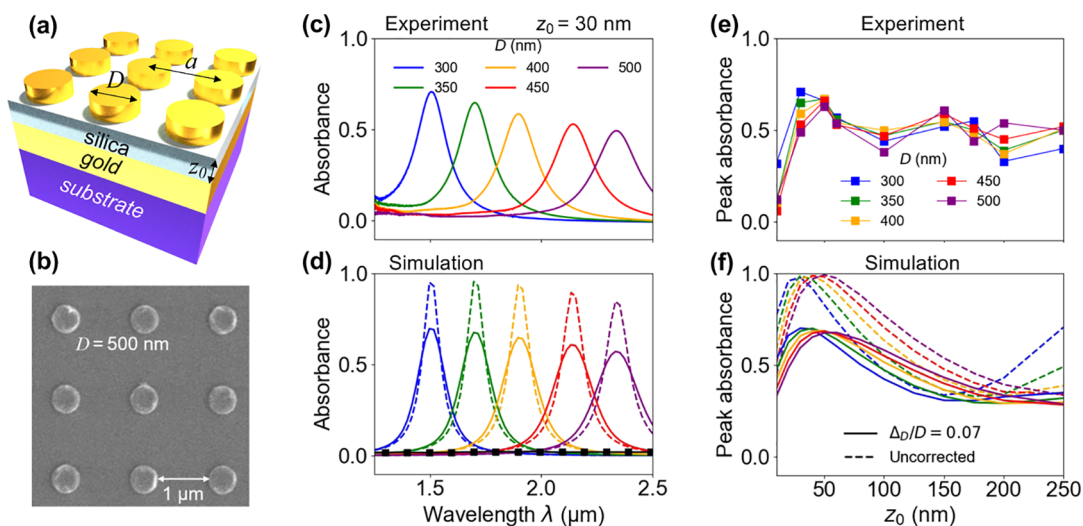

Figure 5. Effect of interdisk interaction in dense periodic disk arrays. (a) Schematic representation of a sample comprising gold disks of diameter D and height 40 nm arranged in a dense periodic square array of period a. The disks lie on a silica layer of thickness z_0 deposited on top of a 100-nm-thick gold film. (b) SEM image of a fabricated sample with $D = 500$ nm disks in an array of period $a = 3\,D$. (c,d) Measured absorbance spectra (c) and simulated spectra (d) for a fixed silica spacer thickness $z_0 = 30$ nm and different values of the disk diameter. The calculated absorbance of the surface without disks (∼2%) is shown in (d) for comparison (symbols). (e,f) Measured (e) and simulated (f) absolute maximum in the absorbance as a function of silica spacer thickness for several disk diameters (see color-coordinated legend in (e)). In panels (d,f), we present simulations for disks of uniform diameter (broken curves) as well as the convolution of spectra obtained for a Gaussian distribution of arrays with different diameters (solid curves; fwhm $\Delta_D = 0.07\,D$; see Figure S7 in the Supporting Information). The central disk diameter in the simulations is increased by 20 nm with respect to the nominal size for $D = 300-400$ nm and by 30 nm for $D = 450-500$ nm, consistent with deviations in the actual diameters of our samples (see Figure S7 in the Supporting Information).

the maximum coupling cross section exceeds the dipolar free-space extinction limit σ_0. Although our samples incorporate a dielectric spacing in contrast to the self-standing particle configuration in the model calculations in Figure 1, the maximum cross section exceeds σ_0 in both cases. In addition, our electromagnetic simulations (Figure 3c, broken curves) reproduce well the magnitude and overall behavior of the coupling cross section as a function of particle−metal surface

distance z_0, although the maximum at $z_0 \sim 150$ nm is better defined in the experiment.

Light Coupling through Periodic Scatterer Arrays. An extension from individual particles to periodic arrays of a small period leads to a depletion of the reflectivity under resonance conditions, as we show theoretically in Figure 4 and experimentally in Figure 5. We first explore this type of configuration through analytical theory for a periodic array of small particles placed at a distance z_0 from a planar surface (see

the self-contained derivation in Methods). The effective polarizability of the particles is still given by eq 2, but with the particle—surface interaction term $\mathcal{G}$ supplemented by the self-consistent interaction with all other particles in the array (see eq 19 in Methods). We then have $\alpha^{\mathrm{eff}} = 1/(\alpha^{-1} - G)$, where $G = G^{\mathrm{dir}} + G^{\mathrm{ref}}$ is the sum of direct and surface-reflected interparticle interactions. In the absence of a surface, direct interactions produce lattice resonances that are observed as maxima in the optical reflectivity,[38,39] including the possibility of complete reflection even for arbitrarily small particles.[40] Although lattice resonances associated with free-space interparticle interactions (i.e., dipolar fields decaying with distance r as $1/r$) are generally quenched when the particles are placed at an interface between different dielectric media,[41,42] a new type of lattice resonance is produced in particle arrays deposited on a polariton-supporting surface,[38] assisted by surface-mode-mediated interparticle interactions (now decaying as $1/\sqrt{r}$ with distance). The separation between the array and the surface then acts as a gauge that controls which of the two mechanisms (direct and surface-reflection lattice resonances) is more efficient. For simplicity, we present results for square arrays of period a smaller than the light wavelength λ, so that nonspecular Bragg reflections are evanescent and vanish in the far field.

To better understand the optical behavior of periodic particle arrays near a planar surface, we show in Figure 4a the absorbance calculated from eq 19 as a function of particle-surface separation z_0 and light wavelength λ assuming lossless particles (i.e., taking $\mathrm{Im}\{-\alpha^{-1}\} = 16\pi^3/3\lambda^3$) that are on-resonance for each choice of z_0 and λ (i.e., setting $\mathrm{Re}\{\alpha^{-1} - G\} = 0$). The plot is dominated by regions of near-unity absorption around a horizontal feature at $\lambda \gtrsim a$ and also around oblique lines. The former is produced by a surface-reflection lattice resonance occurring roughly when the in-plane plasmon wavelength λ_p matches the period $a = 1\ \mu\mathrm{m}$, which corresponds to $\lambda - a \approx 11.7$ nm (from the plasmon dispersion relation $\lambda_p = \lambda / \mathrm{Re}\left\{\sqrt{\epsilon_s/(\epsilon_s + 1)}\right\}$ with ϵ_s standing for the gold permittivity[43]), in excellent agreement with the spectral position of the noted horizontal region. The oblique features originate in Fabry—Perot (FP) resonances, which involve multiple reflections at the surface and the array. We can further analyze them by considering $z_0 \gg a$, such that only specular reflections survive: imposing the above-mentioned conditions for α on eq 19, using the exact result[38] $\mathrm{Im}\{G^{\mathrm{dir}}\} = 4\pi^2/a^2\lambda - 16\pi^3/3\lambda^3$, and evaluating G^{ref} by only retaining the specular beam in eq 18, we obtain a total reflection coefficient $\mathcal{R}_{\mathrm{pp}}^0 = r_p^0 - (r_p^0 e^{ikz_0} - e^{-ikz_0})^2/(\mathrm{Re}\{r_p^0 e^{2ikz_0}\} - 1)$, where the vanishing of the denominator coincides well with the oblique features. This expression for the reflection coefficient produces results that are nearly identical to those in Figure 4a, except for the absence of the horizontal plasmon-mediated feature (see Figure S6 in the Supporting Information). Incidentally, there is a clear interaction between the two types of resonances, leading to avoided crossings as a function of z_0 and λ.

For particles described by the polarizability in eq 1 (Figure 4b−d), we observe a similar set of periodic FP resonances that are redshifted relative to the chosen particle resonance (set to $\lambda_0 = 1.1\ \mu\mathrm{m}$, green arrows) as well as a more involved structure near the surface-reflection resonance, always appearing at a wavelength slightly above the period. For $a = 1\ \mu\mathrm{m}$ (Figure 4b), a redshift is observed in the FP resonances, which show up at a wavelength larger than the period as a consequence of

particle—surface interaction. This behavior can be intuitively understood for large z_0, where full maximum reflection from the particle array alone (associated with the direct lattice resonance) is well-known to take place at a resonant wavelength $\lambda > a$,[38] similar to the resonances identified in metallic gratings by Fano.[44] To be more quantitative, using the polarizability in eq 1, the resonance frequency signaled by $\mathrm{Re}\{\alpha^{-1} - G\} = 0$ occurs at $\omega \approx \omega_0 - (3c^3\kappa/4\omega_0^3)\mathrm{Re}\{G\}$, which is redshifted relative to ω_0 because $\mathrm{Re}\{G\} > 0$ near the lattice resonance.[38] When a approaches λ_0, the redshifted resonance is still separated from the surface mode (Figure 4c). Eventually, for a sufficiently large compared with λ_0 (Figure 4d), the direct and surface-reflection resonances merge, generating an avoided-crossing pattern resembling the one observed in Figure 4a.

We experimentally investigate disk particle arrays near a gold surface under the configuration of Figure 5a with a period a set to three times the disk diameter D (see Figure 5b for an SEM image of an illustrative sample). In contrast to the isolated disks studied above, we consistently observe values of the maximum absorbance around or exceeding 50% that are mildly dependent on disk diameter (Figure 5c). Our electromagnetic simulations for defect-free disks show absorption maxima at similar wavelengths (Figure 5d, broken curves) but with substantially higher peak values nearing full absorbance, in contrast to ∼2% for the surface without disks. We attribute this effect to the finite distribution of disk sizes around the nominal diameter due to fabrication imperfections in the lithography process. As a simple prescription to account for such an effect in theory, we average over the spectra calculated for disk arrays with different diameters (see Figure S7 in the Supporting Information for details), leading to a reduction in peak absorption that results in similar values to those observed in the experiment when assuming a Gaussian diameter distribution with a 7% full-width-at-half-maximum (fwhm) variation (Figure 5d, solid curves). This level of imprecision is consistent with the diameter histograms obtained upon inspection of SEM images of different experimental samples (see Figure S7). The optimum placement of the scatterers needed to optimize light coupling to surface modes is closely related to their self-interaction with the surface, which impacts how they scatter light. In contrast to individual scatterers, self-interaction in the array configuration is supplemented by the interaction of each scatterer with all other particles in the array, thus, substantially changing the optical response of the entire system. Consequently, we expect that the optimum distance should differ in both configurations. Indeed, when analyzing the peak absorption measured as a function of silica spacer thickness for a broad range of disk diameters, we observe an absolute maximum at $z_0 \lesssim 50$ nm (Figure 5e), a much lower distance than for individual particles, where optimum coupling was found at $z_0 \sim 150$ nm. This result is in excellent agreement with simulations when we incorporate the finite distribution of disk diameters (Figure 5f, solid curves), although it represents a departure from the prediction for perfect disks, in which, although the absolute maximum is still lying at $z_0 \lesssim 50$ nm, one finds nearly full absorption. The presence of a peak at low values of z_0 is also in qualitative agreement with the leftmost feature observed in the model system of Figure 4.

■ CONCLUDING REMARKS

In brief, we have experimentally demonstrated a large optical coupling between externally propagating light and modes on a

planar gold surface assisted by individual gold particles placed at an optimum distance from it through a silica spacer. For disks of 40 nm thickness and different diameters, the optimum spacer thickness is ~150 nm, for which we measure a maximum coupling cross section that is about twice the extinction cross section of a lossless resonant dipole in free space ~$\lambda^2/2$. When the particles are arranged in denser periodic arrays with a surface-to-surface disk separation equal to twice the diameter, dramatic changes are produced in the light-to-surface coupling characteristics due to interparticle interaction, such as a departure from the previous distance for optimum coupling down to a smaller separation $z_0 \sim 30$ nm. Our results support the use of dipolar scatterers to assist the coupling between propagating light and surface polaritons, emphasizing the important role played by particle-surface separation to maximize the coupling. In our method, the response of the scatterer is dipolar, as lossless as possible, and resonant at the targeted surface-polariton frequency. An extension of these results to multipolar scatterers should be attainable, in which the maximum coupling cross section at an optimum distance can depend on the scattering properties, and additionally, an engineered combination of different multipolar responses could push the coupling even further. Optimum coupling to surface modes in anisotropic materials[45] (e.g., phonon polaritons in MoO_3) should also be possible by resorting to in-plane anisotropic scatterers. We envision the use of suitably spaced couplers as a practical solution to the in/out-coupling problem in nanophotonics, whereby light can be funneled into surface modes at designated positions, propagate along the surface while performing different functionalities (e.g., optical sensing through absorption by analytes), and eventually be converted back into radiation.

■ METHODS

Fabrication of Gold Films on Silicon Substrates. We deposited gold films on square silicon chips with a 1 cm^2 area. Before the gold deposition, the chips were cleaned in ultrasonic baths of acetone and isopropyl alcohol solvents for 5 min each and covered with a layer of 3 nm of titanium via electron-beam (e-beam) evaporation to promote stronger gold adhesion. Thick gold films (100 nm thickness) were then deposited using thermal evaporation. Both depositions were carried out in a Leybold Univex 350 system at a chamber pressure of 10^{-6} mbar.

Silica Spacer Layer Deposition. A layer of 1 nm of titanium was deposited on gold to improve silica adhesion.[46] A small thickness of the titanium layer was used to minimize additional inelastic losses of surface-plasmon polaritons at the silica/gold interface. A silica layer was then deposited using an ion-assisted e-beam Lesker LAB18 evaporator with different silica thicknesses in the 10−200 nm range on different chips. Finally, samples were annealed at 200 °C for 30 min to improve stability.

E-Beam Nanolithography. Gold nanodisks with different diameters were fabricated by using e-beam lithography (EBL) and a liftoff process of thermally evaporated gold. In this procedure, a 350 nm-thick layer of ZEP520A positive resist was spin-coated onto silica-coated gold mirrors. Samples were then prebaked on a hot plate at 150 °C for 2 min and allowed to cool for 5 min. Following the cooling, disk patterns were inscribed onto the resist using the Crestec CABL 9000C e-beam lithography machine. After EBL, samples were immersed in an amyl acetate developer for 1 min, revealing the desired

hole patterns in the resist. Subsequently, a 3-nm titanium layer and a 40 nm gold layer were successively deposited on the samples using the Leybold Univex 350 system. The resist was then removed by immersing the sample in a warm acetone bath at 70 °C for 15 min, accompanied by gentle blow-cleaning using plastic pipettes. This resulted in gold disk patterns neatly positioned on top of the silica spacer layer. Throughout this work, we report nominal disk diameters, but a variation in diameter of a few percent was observed upon inspection of SEM images (see Figure S7 in the Supporting Information).

SEM Imaging and Optical Characterization. SEM images were collected using a FEG-SEM Inspect-F system operated at 3 kV. Optical reflection spectra were acquired using a Bruker Hyperion FTIR spectrometer covering the wavelength range of 1.2−25 μm with unpolarized light. (Incidentally, polarization should not play a role under normal incidence for the geometries under consideration.)

Theoretical Analysis of the Absorption Cross Section by a Particle Near a Planar Surface. We consider a system comprising a small particle separated by a distance z_0 from a planar surface and illuminated by a light plane wave of frequency ω and electric field amplitude $\mathbf{E}_0^{\text{inc}}$. The particle is taken to be isotropic along directions parallel to the surface and small enough as to be describable in terms of its 3×3 electric polarizability tensor $\alpha(\omega)$, while the surface is accounted for using its Fresnel reflection coefficients $r_{k_\parallel\text{p}}$ and $r_{k_\parallel\text{s}}$ for p (TM) and s (TE) polarization, respectively, which depend on the in-plane optical wave vector $\mathbf{k}_\parallel$. We take the particle position at $\mathbf{r}_0 = (0, 0, z_0)$ with $z_0 > 0$ and the surface at $z = 0$. The convention $\mathbf{E}(\mathbf{r},t) = 2\text{Re}\{\mathbf{E}(\mathbf{r})e^{-i\omega t}\}$ is used for the time dependence of the optical electric field and similarly for other electromagnetic quantities, so we operate with complex amplitudes associated with the $e^{-i\omega t}$ components. Upon illumination, the particle acquires an induced dipole moment $\mathbf{p} = \alpha\mathbf{E}(\mathbf{r}_0)$ in response to the field $\mathbf{E}(\mathbf{r}_0)$ acting on it. The latter is comprised of the incident field and its reflection on the surface, as well as the reflection of the dipole-generated field. We are interested in the $z > 0$ region in what follows, which we take to be filled by a host medium of real permittivity ϵ.

Dipole Field near a Planar Surface. We find it convenient to write the *direct* field produced by the dipole starting from the expression[17]

$$\mathbf{E}_{\text{dip}}^{\text{dir}}(\mathbf{r}) = \frac{1}{\epsilon}[k'^2\mathbf{p} + (\mathbf{p}\cdot\nabla)\nabla]\frac{e^{ik'|\mathbf{r}-\mathbf{r}_0|}}{|\mathbf{r} - \mathbf{r}_0|} \tag{3}$$

where $k = \omega/c$ and $k' = k\sqrt{\epsilon}$. We now use the identity

$$\frac{e^{ik'r}}{r} = \frac{i}{2\pi}\int\frac{d^2\mathbf{k}_\parallel}{k_z'}e^{i\mathbf{k}_\parallel\cdot\mathbf{R}+ik_z'|z|} \tag{4}$$

where $\mathbf{R} = (x, y)$, $\mathbf{k}_\parallel = (k_x, k_y)$, and $k_z' = \sqrt{k'^2 - k_\parallel^2 + i0^+}$ with $\text{Im}\{k_z'\} > 0$. Inserting eq 4 into 3, we find the expression

$$\mathbf{E}_{\text{dip}}^{\text{dir}}(\mathbf{r}) = \frac{i}{2\pi\epsilon}\int\frac{d^2\mathbf{k}_\parallel}{k_z'}[k'^2\mathbf{p} - \mathbf{k}'^\pm(\mathbf{k}'^\pm\cdot\mathbf{p})]e^{i\mathbf{k}_\parallel\cdot\mathbf{R}+ik_z'|z-z_0|} \tag{5}$$

for the direct dipole field, where

$$\mathbf{k}'^\pm = \mathbf{k}_\parallel \pm k_z'\hat{\mathbf{z}} \tag{6a}$$

represents the 3D optical wave vector for upward (+) and downward (−) propagation, corresponding to $z > z_0$ and $z < z_0$

in eq 5, respectively. To deal with the surface, we expand the integrand in a $\mathbf{k}_{\parallel}$-dependent 3D orthogonal frame defined by the unit polarization vectors $\hat{\mathbf{e}}_{\mathbf{k}_{\parallel}s}^{\pm}$ and $\hat{\mathbf{e}}_{\mathbf{k}_{\parallel}p}^{\pm}$ together with the light wave vector $\mathbf{k}'^{\pm}$ inside the host medium of permittivity ϵ. More explicitly, we have

$$\hat{\mathbf{e}}_{\mathbf{k}_{\parallel}s}^{\pm} = \frac{1}{k_{\parallel}}(-k_y\hat{\mathbf{x}} + k_x\hat{\mathbf{y}}) \tag{6b}$$

$$\hat{\mathbf{e}}_{\mathbf{k}_{\parallel}p}^{\pm} = \frac{1}{k'k_{\parallel}}(\pm k_z'\mathbf{k}_{\parallel} - k_{\parallel}^2\hat{\mathbf{z}}) \tag{6c}$$

Incidentally, we have $\hat{\mathbf{e}}_{\mathbf{k}_{\parallel}s}^{+} = \hat{\mathbf{e}}_{\mathbf{k}_{\parallel}s}^{-}$ for s polarization. We then find that the expression in square brackets in eq 5 is orthogonal to $\mathbf{k}'^{\pm}$, while the second term inside it is orthogonal to the polarization vectors. Therefore, projecting on the latter, we obtain

$$\mathbf{E}_{\text{dip}}^{\text{dir}}(\mathbf{r}) = \frac{ik^2}{2\pi}\sum_{\sigma=s,p}\int\frac{d^2\mathbf{k}_{\parallel}}{k_z'}\hat{\mathbf{e}}_{\mathbf{k}_{\parallel}\sigma}^{\pm}(\hat{\mathbf{e}}_{\mathbf{k}_{\parallel}\sigma}^{\pm}\cdot\mathbf{p})e^{i\mathbf{k}_{\parallel}\cdot\mathbf{R}+ik_z'|z-z_0|} \tag{7a}$$

We are now prepared to write the total dipole field $\mathbf{E}_{\text{dip}}(\mathbf{r}) = \mathbf{E}_{\text{dip}}^{\text{dir}}(\mathbf{r}) + \mathbf{E}_{\text{dip}}^{\text{ref}}(\mathbf{r})$ including the *reflection* of the direct component on the surface, which, from eq 7a, can be written as

$$\mathbf{E}_{\text{dip}}^{\text{ref}}(\mathbf{r}) = \frac{ik^2}{2\pi}\sum_{\sigma=s,p}\int\frac{d^2\mathbf{k}_{\parallel}}{k_z'}r_{k_{\parallel}\sigma}\hat{\mathbf{e}}_{\mathbf{k}_{\parallel}\sigma}^{+}(\hat{\mathbf{e}}_{\mathbf{k}_{\parallel}\sigma}^{-}\cdot\mathbf{p})e^{i\mathbf{k}_{\parallel}\cdot\mathbf{R}+ik_z'(z+z_0)} \tag{7b}$$

where we have introduced the polarization-dependent Fresnel coefficients $r_{k_{\parallel}\sigma}$. From eq 7b, we can write $\mathbf{E}_{\text{dip}}^{\text{ref}}(\mathbf{r}_0) = \mathcal{G}\cdot\mathbf{p}$ in terms of the 3 × 3 matrix

$$\mathcal{G} = \frac{ik^2}{2\pi}\sum_{\sigma=s,p}\int\frac{d^2\mathbf{k}_{\parallel}}{k_z'}r_{k_{\parallel}\sigma}\hat{\mathbf{e}}_{\mathbf{k}_{\parallel}\sigma}^{+}\otimes\hat{\mathbf{e}}_{\mathbf{k}_{\parallel}\sigma}^{-}e^{2ik_z'z_0} \tag{8a}$$

$$= \mathcal{G}_{\parallel}(\hat{\mathbf{x}}\otimes\hat{\mathbf{x}} + \hat{\mathbf{y}}\otimes\hat{\mathbf{y}}) + \mathcal{G}_{\perp}\hat{\mathbf{z}}\otimes\hat{\mathbf{z}} \tag{8b}$$

with components

$$\mathcal{G}_{\parallel} = \frac{i}{2\epsilon}\int_0^{\infty}\frac{k_{\parallel}dk_{\parallel}}{k_z'}e^{2ik_z'z_0}(r_{k_{\parallel}s}k'^2 - r_{k_{\parallel}p}k_z'^2) \tag{8c}$$

$$\mathcal{G}_{\perp} = \frac{i}{\epsilon}\int_0^{\infty}\frac{k_{\parallel}^3dk_{\parallel}}{k_z'}e^{2ik_z'z_0}r_{k_{\parallel}p} \tag{8d}$$

where we have used eq 6a for the polarization vectors and performed the integral over the azimuthal angle of $\mathbf{k}_{\parallel}$.

Self-Consistent Dipole under Plane-Wave Illumination. We now consider the particle-near-the-surface system under illumination by a light plane wave of field amplitude $\mathbf{E}^{\text{inc}}(\mathbf{r}) = \mathbf{E}_0^{\text{inc}}e^{i\mathbf{k}_{0\parallel}\cdot\mathbf{R}-ik_{0z}'z}$ (i.e., incident from $z > 0$), where the 0 subscript in $\mathbf{k}_{0\parallel}$ and $k_{0z}' = \sqrt{k'^2 - k_{0\parallel}^2 + i0^+}$ indicates that these quantities refer to the direction of incidence. The self-consistent field acting on the particle becomes

$$\mathbf{E}(\mathbf{r}_0) = \mathbf{E}_0^{\text{inc}}e^{-ik_{0z}'z_0} + \mathbf{E}_0^{\text{ref}}e^{ik_{0z}'z_0} + \mathbf{E}_{\text{dip}}^{\text{ref}}(\mathbf{r}_0) \tag{9}$$

where $\mathbf{E}_0^{\text{ref}}(\mathbf{r}) = \mathbf{E}_0^{\text{ref}}e^{i\mathbf{k}_{0\parallel}\cdot\mathbf{R}+ik_{0z}'z}$ with

$$\mathbf{E}_0^{\text{ref}} = \sum_{\sigma=s,p}r_{\sigma}^0\hat{\mathbf{e}}_{\mathbf{k}_{0\parallel}\sigma}^{+}(\hat{\mathbf{e}}_{\mathbf{k}_{0\parallel}\sigma}^{-}\cdot\mathbf{E}_0^{\text{inc}}) \tag{10}$$

is the surface-reflected field (involving the Fresnel coefficients $r_{\sigma}^0 \equiv r_{k_{0\parallel}\sigma}$ for a parallel wave vector $\mathbf{k}_{0\parallel}$), while the $\mathbf{E}_{\text{dip}}^{\text{ref}}(\mathbf{r}_0)$ component is linear in the induced dipole according to eq 7b. Note that $\mathbf{E}(\mathbf{r}_0)$ does not include the direct dipole field. Using eq 9 together with $\mathbf{p} = \alpha\cdot\mathbf{E}(\mathbf{r}_0)$ and $\mathbf{E}_{\text{dip}}^{\text{ref}}(\mathbf{r}_0) = \mathcal{G}\cdot\mathbf{p}$ (see eqs 8a, 8b, 8c, and 8d), we find

$$\mathbf{p} = \alpha^{\text{eff}}\cdot(\mathbf{E}_0^{\text{inc}}e^{-ik_{0z}'z_0} + \mathbf{E}_0^{\text{ref}}e^{ik_{0z}'z_0}) \tag{11}$$

for the self-consistently induced dipole, where $\alpha^{\text{eff}} = 1/(\alpha^{-1} - \mathcal{G})$ is the effective polarizability (eq 2).

Optical Theorem and Absorption Cross Section. We consider the time-averaged Poynting vector defined by $\mathbf{S}(\mathbf{r}) = (c/2\pi)\text{Re}\{\mathbf{E}^{\text{scat}}(\mathbf{r}) \times [\mathbf{H}^{\text{scat}}(\mathbf{r})]^*\}$, which is associated with the scattered electric far-field

$$\mathbf{E}^{\text{scat}}(\mathbf{r}) = \mathbf{E}_0^{\text{ref}}e^{i\mathbf{k}_{0\parallel}\cdot\mathbf{R}+ik_{0z}'z} + \mathbf{f}_{\text{dip}}(\hat{\mathbf{r}})\frac{e^{ik'r}}{r} \tag{12}$$

and the corresponding magnetic field $\mathbf{H}^{\text{scat}}(\mathbf{r}) = (1/ik)\nabla \times \mathbf{E}^{\text{scat}}(\mathbf{r})$, where $\mathbf{E}_0^{\text{ref}}$ is the direct surface-reflected field amplitude (eq 10) and $\mathbf{f}_{\text{dip}}(\hat{\mathbf{r}})$ is the scattering amplitude produced by the induced dipole and its reflection on the surface (i.e., $\mathbf{E}_{\text{dip}}(\mathbf{r}) \xrightarrow{k'r\to\infty} \mathbf{f}_{\text{dip}}(\hat{\mathbf{r}})e^{ik'r}/r$). The latter can be analytically obtained from eqs 7a and 7b by applying the identity

$$\int\frac{d^2\mathbf{k}_{\parallel}}{k_z'}e^{i\mathbf{k}_{\parallel}\cdot\mathbf{R}+ik_z'z}g(\mathbf{k}_{\parallel}) \xrightarrow{k'r\to\infty} -2\pi ig(k'\mathbf{R}/r)\frac{e^{ik'r}}{r}$$

leading to the result

$$\mathbf{f}_{\text{dip}}(\hat{\mathbf{r}}) = k^2\sum_{\sigma=s,p}\hat{\mathbf{e}}_{\mathbf{k}_{\parallel}\sigma}^{+}\Big[(\hat{\mathbf{e}}_{\mathbf{k}_{\parallel}\sigma}^{+}e^{-ik_z'z_0} + r_{k_{\parallel}\sigma}\hat{\mathbf{e}}_{\mathbf{k}_{\parallel}\sigma}^{-}e^{ik_z'z_0})\cdot\mathbf{p}\Big] \tag{13}$$

with $\mathbf{k}' = k'\hat{\mathbf{r}}$, under the assumptions that ϵ is real and $z \gg z_0$.

In the absence of the particle, the incident light power ($\mathcal{P}_0 = I_0A\cos\theta_0$, where $I_0 = (c\sqrt{\epsilon}/2\pi)|E_0^{\text{inc}}|^2$ is the associated intensity, A is the surface area, and $\theta_0 = \cos^{-1}(k_{0z}'/k')$ is the incidence angle) is decomposed into reflection and absorption channels as $\mathcal{P}_0 = \mathcal{P}_0^{\text{ref}} + \mathcal{P}_0^{\text{abs}}$, where $\mathcal{P}_0^{\text{ref}} = \mathcal{P}_0|E_0^{\text{ref}}/E_0^{\text{inc}}|^2$, while $\mathcal{P}_0^{\text{abs}}$ is determined by energy conservation (e.g., $\mathcal{P}_0^{\text{abs}} = \mathcal{P}_0(1 - |r_{\sigma}^0|^2)$ for light with polarization σ). (Incidentally, the absorption term is considered to include light transmission for partially transparent substrates; therefore, we only deal with the $z > 0$ region above the surface.)

In the presence of the particle, we can calculate the total power $\mathcal{P}^{\text{ref}}$ reflected by the particle-surface system (i.e., including scattering by the dipole) by integrating the z component of the Poynting vector associated with the field in eq 12 over in-plane coordinates $\mathbf{R}$ at a distant constant-z plane. This leads to (see the Supporting Information)

$$\mathcal{P}^{\text{ref}} = \mathcal{P}_0^{\text{ref}} + \sigma^{\text{scat}}I_0 - \sigma^{\text{ext}}I_0 \tag{14}$$

where we recover $\mathcal{P}_0^{\text{ref}}$ from the contribution of the $\mathbf{E}_0^{\text{ref}}$ term alone and we define the cross sections σ^{scat} and σ^{ext} arising from $\mathbf{f}_{\text{dip}}(\hat{\mathbf{r}})$ and its interference with $\mathbf{E}_0^{\text{ref}}$, respectively. More precisely, we can write $\sigma^{\text{scat}} = \int d\Omega_{\hat{\mathbf{r}}}\sigma^{\text{scat}}(\hat{\mathbf{r}})$ in terms of an elastic *scattering* cross section resolved into outgoing directions $\hat{\mathbf{r}}$ as

$$\sigma^{\text{scat}}(\hat{\mathbf{r}}) = |\mathbf{f}_{\text{dip}}(\hat{\mathbf{r}})/E_0^{\text{inc}}|^2 \tag{15a}$$

where $\mathbf{f}_{\text{dip}}(\hat{\mathbf{r}})$ is given by eq 13. The interference term accounts for the fraction of incident power that is not recovered through specular reflection or nonspecular elastic scattering, so it can be interpreted as an *extinction* cross section

$$\sigma^{\text{ext}} = \frac{4\pi}{k'|E_0^{\text{inc}}|^2}\text{Im}\{\mathbf{f}_{\text{dip}}(\hat{\mathbf{k}}_0^+)\cdot\mathbf{E}_0^{\text{ref}*}\} \tag{15b}$$

where we define $\hat{\mathbf{k}}_0^{\pm} = (1/k')(\mathbf{k}_{0\parallel} \pm k'_{0z}\hat{\mathbf{z}})$ to indicate the direction of incidence $(-)$ and specular reflection $(+)$. A detailed derivation of eqs 15a and 15b is offered in Section S1 of the Supporting Information. Finally, energy conservation leads to $\mathcal{P}_0 = \mathcal{P}^{\text{ref}} + \mathcal{P}^{\text{abs}}$, where the absorbed power $\mathcal{P}^{\text{abs}} = \mathcal{P}_0^{\text{abs}} + \sigma^{\text{abs}}I_0$ can be in turn separated into the sum of a contribution $\mathcal{P}_0^{\text{abs}}$ arising in the absence of the particle (see above) and a component induced by the presence of the particle, which we express in terms of an *absorption* cross section σ^{abs}. Combining these elements, we have

$$\sigma^{\text{abs}} = \sigma^{\text{ext}} - \sigma^{\text{scat}} \tag{15c}$$

We note that σ^{abs} accounts for absorption events that take place either at the surface or at the dipole. The latter can be readily obtained from the field acting on the particle as[47]

$$\sigma_{\text{dip}}^{\text{abs}} = \frac{4\pi}{k'}\left[\text{Im}\{\alpha\} - \frac{2k'^3}{3\epsilon}|\alpha|^2\right]|\mathbf{E}(\mathbf{r}_0)/E_0^{\text{inc}}|^2 \tag{16}$$

which vanishes in the lossless limit[37] $(\text{Im}\{-1/\alpha\} = 2k'^3/3\epsilon)$. The power absorbed by the surface is finally given by $\sigma^{\text{abs}} - \sigma_{\text{dip}}^{\text{abs}}$.

Incidentally, in the absence of a substrate, eq 15a remains valid for the angle-dependent scattering cross section by an electric dipolar scatterer. Additionally, a direct extrapolation of the above analysis shows that eq 15b yields the extinction by an isolated particle in a homogeneous medium if we substitute $\hat{\mathbf{k}}_0^-$ for $\hat{\mathbf{k}}_0^+$ and $\mathbf{E}^{\text{inc}*}$ for $\mathbf{E}_0^{\text{ref}*}$.

It is worth noting that the total reflected power $\mathcal{P}^{\text{ref}}$ in eq 14 deviates from the one for the surface without a particle $\mathcal{P}_0^{\text{ref}}$ (upon light-plane-wave illumination) because it involves the subtraction of the change in absorption power $\sigma^{\text{abs}}I_0$ (see eq 15c). In addition, the extinction cross section σ^{ext} relates to the reduction produced in the specularly reflected beam by introducing the particle, whereas σ^{scat} refers to the resulting nonspecular reflection. Analogous cross sections are commonly employed to characterize free-standing particles, relating to the depletion and deflection from an incident light plane wave and, consequently, satisfying the inequality $\sigma^{\text{ext}} \geq \sigma^{\text{scat}}$ because extinction is the sum of scattering and absorption. In contrast to the free-standing scatterer, for which all cross sections are positive-defined, the inequality above does not hold for the particle-surface system, which can feature negative values of σ^{ext} (see Figure 1c), indicating that the particle redirects light to the specularly reflected beam at the expense of a reduction in absorption by the planar surface, while σ^{scat} remains always positive.

Under normal incidence, eqs 15a and 15b reduce to

$$\sigma^{\text{scat}} = \pi k^4 |\alpha_{\parallel}^{\text{eff}}|^2 \, |1 - r_p^0 e^{2ik'z_0}|^2$$
$$\times \int_0^1 d\mu[|1 + r_{k_{\parallel}s}e^{2ik'z_0\mu}|^2 + |1 - r_{k_{\parallel}p}e^{2ik'z_0\mu}|^2\mu^2] \tag{17a}$$

$$\sigma^{\text{ext}} = \frac{4\pi k}{\sqrt{\epsilon}}\text{Im}\left\{-\alpha_{\parallel}^{\text{eff}}(1 - r_p^0 e^{2ik'z_0})^2(r_p^0)^*e^{-2ik'z_0}\right\} \tag{17b}$$

with $\alpha_{\parallel}^{\text{eff}} = 1/(\alpha_{\parallel}^{-1} - \mathcal{G}_{\parallel})$, where $\alpha_{\parallel}$ stands for the in-plane component of the polarizability tensor and $k_{\parallel} = k'\sqrt{1 - \mu^2}$. We use eqs 17a and 17b to produce Figure 1b,c for a lossless scatterer $(\sigma_{\text{dip}}^{\text{abs}} = 0)$ near a gold surface described by a permittivity $\epsilon_s(\omega)$ taken from optical data,[43] so that $r_p^0 = (\sqrt{\epsilon_s} - 1)/(\sqrt{\epsilon_s} + 1)$, $r_{k_{\parallel}s} = (\mu - \mu_s)/(\mu + \mu_s)$, $r_{k_{\parallel}p} = (\epsilon_s\mu - \mu_s)/(\epsilon_s\mu + \mu_s)$, and $\mu_s = \sqrt{\epsilon_s + \mu^2 - 1}$.

Theoretical Analysis of the Absorbance by a Periodic Particle Array Near a Planar Surface. We now extend the above analysis to a periodic array of particles placed at positions $(\mathbf{R}_j, z_0)$ with one of the lattice sites $(j = 0)$ set at origin $\mathbf{R}_0 = 0$. For light incident with in-plane wave vector $\mathbf{k}_{0\parallel}$, the dipole induced on the particle at each lattice site j can be written as $\mathbf{p}e^{i\mathbf{k}_{0\parallel}\cdot\mathbf{R}_j}$. Following the methods of ref 38, we find the induced dipole $\mathbf{p}$ to be given by eq 11, but with the effective polarizability redefined as $\alpha^{\text{eff}} = 1/[\alpha^{-1} - G(\mathbf{k}_{0\parallel})]$, such that $\mathcal{G}$ is substituted by a lattice sum $G(\mathbf{k}_{0\parallel})$ over the fields induced by the dipoles of all particles in the array. We can separate the lattice sum as $G(\mathbf{k}_{0\parallel}) = G^{\text{dir}}(\mathbf{k}_{0\parallel}) + G^{\text{ref}}(\mathbf{k}_{0\parallel})$ into the contributions of direct and surface-reflected parts. In particular, we have $G^{\text{dir}}(\mathbf{k}_{0\parallel}) = \sum_{j\neq 0} e^{-i\mathbf{k}_{0\parallel}\cdot\mathbf{R}_j}\mathbf{E}_{\text{dip}}^{\text{dir}}(\mathbf{R}_j, z_0)$ (see eq 3), in which the self-induced term $j = 0$ is not included. We evaluate $G^{\text{dir}}(\mathbf{k}_{0\parallel})$ numerically using highly convergent methods developed by Kambe.[48,49] The surface-reflected component can be directly obtained from eq 7b as $G^{\text{ref}}(\mathbf{k}_{0\parallel}) = \sum_j e^{-i\mathbf{k}_{0\parallel}\cdot\mathbf{R}_j}\mathbf{E}_{\text{dip}}^{\text{ref}}(\mathbf{R}_j, z_0)$, where the $j = 0$ term (self-interaction) now needs to be included and is found to reduce to the single-particle self-interaction $\mathcal{G}$ (eqs 8a, 8b, 8c, and 8d). We carry out the j sum by using the identity $\sum_j e^{i\mathbf{k}_{\parallel}\cdot\mathbf{R}_j} = (2\pi)^2 A^{-1}\sum_{\mathbf{g}}\delta(\mathbf{k}_{\parallel} - \mathbf{g})$, where A is the unit-cell area and the rightmost sum runs over 2D reciprocal lattice vectors $\mathbf{g}$. This allows us to write

$$G^{\text{ref}}(\mathbf{k}_{0\parallel}) = \frac{2\pi i k^2}{A}\sum_{\mathbf{g},\sigma}\frac{e^{2ik'_{\mathbf{g}z}z_0}}{k'_{\mathbf{g}z}}r_{|\mathbf{k}_{0\parallel}+\mathbf{g}|,\sigma}\hat{\mathbf{e}}_{\mathbf{k}_{0\parallel}+\mathbf{g},\sigma}^+ \otimes \hat{\mathbf{e}}_{\mathbf{k}_{0\parallel}+\mathbf{g},\sigma}^- \tag{18}$$

where $k'_{\mathbf{g}z} = \sqrt{k^2\epsilon - |\mathbf{k}_{0\parallel} + \mathbf{g}|^2 + i0^+}$. We evaluate this expression by direct numerical computation, producing convergent results by including $\mathbf{g}$ vectors of large magnitude compared with both k' and $1/z_0$. Now, the total reflected field is given by

$$\mathbf{E}^{\text{ref}}(\mathbf{r}) = \mathbf{E}_0^{\text{ref}}(\mathbf{r})$$
$$+ \sum_j e^{i\mathbf{k}_{0\parallel}\cdot\mathbf{R}_j}\left[\mathbf{E}_{\text{dip}}^{\text{dir}}(\mathbf{r} - \mathbf{R}_j) + \mathbf{E}_{\text{dip}}^{\text{ref}}(\mathbf{r} - \mathbf{R}_j)\right]$$

where we include the direct reflection on the surface (eq 10) as well as the direct and surface-reflected fields produced by each of the dipoles (eqs 7a and 7b). Finally, using eqs 7a, 7b, 10,

and 11, and transforming the j sum into a $\mathbf{g}$ sum as indicated above, we obtain

$$\mathbf{E}^{\text{ref}}(\mathbf{r}) = \sum_{\mathbf{g},\sigma\sigma'} \mathcal{R}^{\mathbf{g}}_{\sigma\sigma'} \hat{\mathbf{e}}^+_{\mathbf{k}_{0\parallel}+\mathbf{g},\sigma}(\hat{\mathbf{e}}^-_{\mathbf{k}_{0\parallel}\sigma'} \cdot \mathbf{E}^{\text{inc}}_0) e^{i(\mathbf{k}_{0\parallel}+\mathbf{g})\cdot\mathbf{R}+ik'_{\mathbf{g}z}z}$$

which consists of different Bragg reflections labeled by reciprocal lattice vectors $\mathbf{g}$ and transforming an incident polarization σ' into σ according to the coefficients

$$\mathcal{R}^{\mathbf{g}}_{\sigma\sigma'} = \delta_{\mathbf{g},0}\delta_{\sigma,\sigma'} \, r^0_\sigma + \frac{2\pi i k^2}{A k'_{\mathbf{g}z}} e^{-i(k'_{\mathbf{g}z}+k'_{0z})z_0}$$

$$\times \left[(\tilde{\alpha}^{+-}_{\mathbf{g},\sigma\sigma'} + r^0_{\sigma'} \, \tilde{\alpha}^{++}_{\mathbf{g},\sigma\sigma'} \, e^{2ik'_{0z}z_0}) \right.$$

$$\left. + (\tilde{\alpha}^{--}_{\mathbf{g},\sigma\sigma'} + r^0_\sigma \tilde{\alpha}^{-+}_{\mathbf{g},\sigma\sigma'} e^{2ik'_{0z}z_0}) r_{|\mathbf{k}_{0\parallel}+\mathbf{g}|,\sigma} e^{2ik'_{\mathbf{g}z}z_0} \right]$$

where the particle response enters through the matrix elements $\tilde{\alpha}^{ss'}_{\mathbf{g},\sigma\sigma'} = \hat{\mathbf{e}}^s_{\mathbf{k}_{0\parallel}+\mathbf{g},\sigma} \cdot [\alpha^{-1} - G(\mathbf{k}_{0\parallel})]^{-1} \cdot \hat{\mathbf{e}}^{s'}_{\mathbf{k}_{0\parallel}\sigma'}$. Bragg reflections for $g > k'$ produce evanescent fields, and in particular, for k' smaller than the minimum $g \neq 0$, we are left in the diffractionless regime, where only the specularly reflected beam ($\mathbf{g} = 0$ term) survives in the far field, so we have $\mathbf{E}^{\text{ref}}(\mathbf{r}) = \mathbf{E}^{\text{ref}} e^{i\mathbf{k}_{0\parallel}\cdot\mathbf{R}+ik'_{0z}z}$ with

$$\mathbf{E}^{\text{ref}} = \sum_{\sigma\sigma'} \mathcal{R}^0_{\sigma\sigma} \hat{\mathbf{e}}^+_{\mathbf{k}_{0\parallel}\sigma}(\hat{\mathbf{e}}^-_{\mathbf{k}_{0\parallel}\sigma'} \cdot \mathbf{E}^{\text{inc}}_0)$$

In Figure 4, we consider a square lattice of period $a < \lambda$ irradiated by normally incident p-polarized light with $\mathbf{E}^{\text{inc}}_0$ along a principal lattice direction $\hat{\mathbf{x}}$, and therefore, the reflected field amplitude reduces to $\mathbf{E}^{\text{ref}} = -\mathcal{R}^0_{\text{pp}}\mathbf{E}^{\text{inc}}_0$, where

$$\mathcal{R}^0_{\text{pp}} = r^0_{\text{p}} - \frac{2\pi i k}{a^2\sqrt{\epsilon}} \frac{(r^0_{\text{p}} e^{ik'z_0} - e^{-ik'z_0})^2}{\alpha^{-1}_\parallel - G_{xx}(0)} \tag{19}$$

is the reflection coefficient of the entire system.

ASSOCIATED CONTENT

Ⓢ Supporting Information

The Supporting Information is available free of charge at https://pubs.acs.org/doi/10.1021/acsphotonics.3c01742.

> Detailed derivation of eqs 15a, 15b and 15c, optical theorem for a dipolar scatterer near a planar surface, extinction and scattering cross sections under the conditions of Figure 1, optical near-field for point-dipole and gold-disk particles near a planar gold surface, fits of experiments to the effective polarizability, optical theorem for a particle near a gold surface, measured absorption cross sections, effect of surface-reflection lattice resonances on the absorption by periodic particle arrays near a gold surface, effect of particle-size distribution on the absorbance of periodic disk arrays (PDF)

AUTHOR INFORMATION

Corresponding Authors

Vahagn Mkhitaryan − ICFO-Institut de Ciencies Fotoniques, The Barcelona Institute of Science and Technology, 08860 Castelldefels (Barcelona), Spain; Email: vmkhit@gmail.com

F. Javier García de Abajo − ICFO-Institut de Ciencies Fotoniques, The Barcelona Institute of Science and Technology, 08860 Castelldefels (Barcelona), Spain; ICREA-

Institució Catalana de Recerca i Estudis Avançats, 08010 Barcelona, Spain; Ⓞorcid.org/0000-0002-4970-4565; Email: javier.garciadeabajo@nanophotonics.es

Authors

Saad Abdullah − ICFO-Institut de Ciencies Fotoniques, The Barcelona Institute of Science and Technology, 08860 Castelldefels (Barcelona), Spain

Eduardo J. C. Dias − ICFO-Institut de Ciencies Fotoniques, The Barcelona Institute of Science and Technology, 08860 Castelldefels (Barcelona), Spain; Ⓞorcid.org/0000-0002-6347-5631

Jan Krpenský − ICFO-Institut de Ciencies Fotoniques, The Barcelona Institute of Science and Technology, 08860 Castelldefels (Barcelona), Spain; Ⓞorcid.org/0000-0002-1188-9349

Complete contact information is available at: https://pubs.acs.org/10.1021/acsphotonics.3c01742

Notes

The authors declare no competing financial interest.

■ REFERENCES

(1) Liang, Z.; Sun, J.; Jiang, Y.; Jiang, L.; Chen, X. Plasmonic enhanced optoelectronic devices. *Plasmonics* **2014**, *9*, 859−866.

(2) Baugher, B. W. H.; Churchill, H. O. H.; Yang, Y.; Jarillo-Herrero, P. Optoelectronic devices based on electrically tunable p-n diodes in a monolayer dichalcogenide. *Nat. Nanotechnol.* **2014**, *9*, 262−267.

(3) McFarland, A. D.; Van Duyne, R. P. Single silver nanoparticles as real-time optical sensors with zeptomole sensitivity. *Nano Lett.* **2003**, *3*, 1057−1062.

(4) Cetin, A. E.; Altug, H. Fano resonant ring/disk plasmonic nanocavities on conducting substrates for advanced biosensing. *ACS Nano* **2012**, *6*, 9989−9995.

(5) Saeidi, P.; Jakoby, B.; Pühringer, G.; Tortschanoff, A.; Stocker, G.; Dubois, F.; Spettel, J.; Grille, T.; Jannesari, R. Designing mid-infrared gold-based plasmonic slot waveguides for CO_2-sensing applications. *Sensors* **2021**, *21*, 2669.

(6) Genevet, P.; Tetienne, J. P.; Gatzogiannis, E.; Blanchard, R.; Kats, M. A.; Scully, M. O.; Capasso, F. Large enhancement of nonlinear optical phenomena by plasmonic nanocavity gratings. *Nano Lett.* **2010**, *10*, 4880−4883.

(7) Kauranen, M.; Zayats, A. V. Nonlinear plasmonics. *Nat. Photonics* **2012**, *6*, 737−748.

(8) Panoiu, N. C.; Sha, W. E. I.; Lei, D. Y.; Li, G.-C. Nonlinear optics in plasmonic nanostructures. *J. Opt.* **2018**, *20*, 083001.

(9) Alvarez-Puebla, R.; Liz-Marzán, L. M.; García de Abajo, F. J. Light concentration at the nanometer scale. *J. Phys. Chem. Lett.* **2010**, *1*, 2428−2434.

(10) Yang, X.; Sun, Z.; Low, T.; Hu, H.; Guo, X.; García de Abajo, F. J.; Avouris, P.; Dai, Q. Nanomaterial-based plasmon-enhanced infrared spectroscopy. *Adv. Mater.* **2018**, *30*, 1704896.

(11) Kneipp, K.; Wang, Y.; Kneipp, H.; Perelman, L. T.; Itzkan, I.; Dasari, R. R.; Feld, M. S. Single molecule detection using surface-enhanced Raman scattering (SERS). *Phys. Rev. Lett.* **1997**, *78*, 1667−1670.

(12) Xu, H.; Bjerneld, E. J.; Käll, M.; Börjesson, L. Spectroscopy of single hemoglobin molecules by surface enhanced Raman scattering. *Phys. Rev. Lett.* **1999**, *83*, 4357−4360.

(13) Rodríguez-Lorenzo, L.; Álvarez-Puebla, R. A.; Pastoriza-Santos, I.; Mazzucco, S.; Stéphan, O.; Kociak, M.; Liz-Marzán, L. M.; García de Abajo, F. J. Zeptomol detection through controlled ultrasensitive surface-enhanced Raman scattering. *J. Am. Chem. Soc.* **2009**, *131*, 4616−4618.

(14) Atwater, H. A.; Polman, A. Plasmonics for improved photovoltaic devices. *Nat. Mater.* **2010**, *9*, 205−213.

(15) Shen, W.; Zhao, G.; Zhang, X.; Bu, F.; Yun, J.; Tang, J. Using dual microresonant cavity and plasmonic effects to enhance the photovoltaic efficiency of flexible polymer solar cells. *Nanomaterials* **2020**, *10*, 944.

(16) Echarri, A. R.; Cox, J. D.; Yu, R.; García de Abajo, F. J. Enhancement of nonlinear optical phenomena by localized resonances. *ACS Photonics* **2018**, *5*, 1521−1527.

(17) Dias, E. J. C.; García de Abajo, F. J. Fundamental Limits to the Coupling between Light and 2D Polaritons by Small Scatterers. *ACS Nano* **2019**, *13*, 5184−5197.

(18) Akimov, A. V.; Mukherjee, A.; Yu, C. L.; Chang, D. E.; Zibrov, A. S.; Hemmer, P. R.; Park, H.; Lukin, M. D. Generation of single optical plasmons in metallic nanowires coupled to quantum dots. *Nature* **2007**, *450*, 402−406.

(19) Chang, D. E.; Vuletić, V.; Lukin, M. D. Quantum nonlinear optics photon by photon. *Nat. Photonics* **2014**, *8*, 685−694.

(20) Lambe, J.; McCarthy, S. L. Light emission from inelastic electron tunneling. *Phys. Rev. Lett.* **1976**, *37*, 923−925.

(21) Leon, C. C.; Gunnarsson, O.; de Oteyza, D. G.; Roslawska, A.; Merino, P.; Grewal, A.; Kuhnke, K.; Kern, K. Single photon emission from a plasmonic light source driven by a local field-induced Coulomb blockade. *ACS Nano* **2020**, *14*, 4216−4223.

(22) Wang, L.; Papadopoulos, S.; Iyikanat, F.; Zhang, J.; Huang, J.; Taniguchi, T.; Watanabe, K.; Calame, M.; Perrin, M. L.; García de Abajo, F. J.; Novotny, L. Exciton-assisted electron tunnelling in van der Waals heterostructures. *Nat. Mater.* **2023**, *22*, 1094−1099.

(23) García de Abajo, F. J. Optical excitations in electron microscopy. *Rev. Mod. Phys.* **2010**, *82*, 209−275.

(24) Polman, A.; Kociak, M.; García de Abajo, F. J. Electron-beam spectroscopy for nanophotonics. *Nat. Mater.* **2019**, *18*, 1158−1171.

(25) Powell, C. J.; Swan, J. B. Origin of the characteristic electron energy losses in aluminum. *Phys. Rev.* **1959**, *115*, 869−875.

(26) Pettit, R. B.; Silcox, J.; Vincent, R. Measurement of surface-plasmon dispersion in oxidized aluminum films. *Phys. Rev. B: Solid State* **1975**, *11*, 3116−3123.

(27) Garcíia de Abajo, F. J. Multiple excitation of confined graphene plasmons by single free electrons. *ACS Nano* **2013**, *7*, 11409−11419.

(28) Boroviks, S.; Wolff, C.; Linnet, J.; Yang, Y.; Todisco, F.; Roberts, A. S.; Bozhevolnyi, S. I.; Hecht, B.; Mortensen, N. A. Interference in edge-scattering from monocrystalline gold flakes [Invited]. *Opt. Mater. Express* **2018**, *8*, 3688−3697.

(29) Marchetti, R.; Lacava, C.; Carroll, L.; Gradkowski, K.; Minzioni, P. Coupling strategies for silicon photonics integrated chips [Invited]. *Photon. Res.* **2019**, *7*, 201−239.

(30) Kretschmann, E.; Raether, H. Notizen: Radiative Decay of Non Radiative Surface Plasmons Excited by Light. *Z. Naturforsch. A* **1968**, *23*, 2135−2136.

(31) Vinogradov, A. P.; Dorofeenko, A. V.; Pukhov, A. A.; Lisyansky, A. A. Exciting surface plasmon polaritons in the Kretschmann configuration by a light beam. *Phys. Rev. B* **2018**, *97*, 235407.

(32) Giles, A. J.; Dai, S.; Glembocki, O. J.; Kretinin, A. V.; Sun, Z.; Ellis, C. T.; Tischler, J. G.; Taniguchi, T.; Watanabe, K.; Fogler, M. M.; Novoselov, K. S.; Basov, D. N.; Caldwell, J. D. Imaging of Anomalous Internal Reflections of Hyperbolic Phonon-Polaritons in Hexagonal Boron Nitride. *Nano Lett.* **2016**, *16*, 3858−3865.

(33) Novotny, L.; Pohl, D. W.; Hecht, B. Light confinement in scanning near-field optical microscopy. *Ultramicroscopy* **1995**, *61*, 1−9.

(34) Keilmann, F.; Hillenbrand, R.; Zayats, A.; Richard, D. Near-field microscopy by elastic light scattering from a tip. *Philos. Trans. R. Soc., A* **2004**, *362*, 787−805.

(35) Cheng, L.; Mao, S.; Li, Z.; Han, Y.; Fu, H. Y. Grating Couplers on Silicon Photonics: Design Principles, Emerging Trends and Practical Issues. *Micromachines* **2020**, *11*, 666.

(36) Joseph, S.; Sarkar, S.; Joseph, J. Grating-coupled surface plasmon-polariton sensing at a flat metal−analyte interface in a hybrid-configuration. *ACS Appl. Mater. Interfaces* **2020**, *12*, 46519−46529.

(37) Dias, E. J. C.; García de Abajo, F. J. Complete coupling of focused light to surface polaritons. *Optica* **2021**, *8*, 520−531.

(38) García de Abajo, F. J. Colloquium: light scattering by particle and hole arrays. *Rev. Mod. Phys.* **2007**, *79*, 1267−1290.

(39) Auguié, B.; Barnes, W. L. Collective resonances in gold nanoparticle arrays. *Phys. Rev. Lett.* **2008**, *101*, 143902.

(40) García de Abajo, F. J.; Gómez-Medina, R.; Sáenz, J. J. Full transmission through perfect-conductor subwavelength hole arrays. *Phys. Rev. E: Stat., Nonlinear, Soft Matter Phys.* **2005**, *72*, 016608.

(41) Bendaña, X. M.; García de Abajo, F. J.; Polman, A. Confined collective excitations of self-standing and supported planar periodic particle arrays. *Opt. Express* **2009**, *17*, 18826−18835.

(42) Auguié, B.; Bendaña, X. M.; Barnes, W. L.; García de Abajo, F. J. Diffractive arrays of gold nanoparticles near an interface: critical role of the substrate. *Phys. Rev. B: Condens. Matter Mater. Phys.* **2010**, *82*, 155447.

(43) Johnson, P. B.; Christy, R. W. Optical constants of the noble metals. *Phys. Rev. B: Solid State* **1972**, *6*, 4370−4379.

(44) Fano, U. Some theoretical considerations on anomalous diffraction gratings. *Phys. Rev.* **1936**, *50*, 573.

(45) Guo, X.; Lyu, W.; Chen, T.; Luo, Y.; Wu, C.; Yang, B.; Sun, Z.; García de Abajo, F. J.; Yang, X.; Dai, Q. Polaritons in Van der Waals heterostructures. *Adv. Mater.* **2023**, *35*, 2201856.

(46) Mostrou, S.; Newton, M. A.; Tarcevski, A.; Nagl, A.; Föttinger, K.; van Bokhoven, J. A. Titanium-anchored gold on silica for enhanced catalytic activity in aqueous ethanol oxidation. *Ind. Eng. Chem. Res.* **2021**, *60*, 1564−1575.

(47) Jackson, J. D. *Classical Electrodynamics*; Wiley: New York, 1999.

(48) Kambe, K. Theory of low-energy electron diffraction. II. Cellular method for complex monolayers and multilayers. *Z. Naturforsch. A* **1968**, *23*, 1280−1294.

(49) Pendry, J. B. *Low Energy Electron Diffraction*; Academic Press: London, 1974.